Lab on a Chip

PAPER

View Article Online
View Journal | View Issue

Cite this: *Lab Chip*, 2014, **14**, 2565

Continuous-flow microfluidic blood cell sorting for unprocessed whole blood using surface-micromachined microfiltration membranes†

Xiang Li,[ab] Weiqiang Chen,[ab] Guangyu Liu,[b] Wei Lu[b] and Jianping Fu*[abc]

Received 20th March 2014,
Accepted 6th May 2014

DOI: 10.1039/c4lc00350k

www.rsc.org/loc

White blood cells (WBCs) constitute about 0.1% of the blood cells, yet they play a critical role in innate and adaptive immune responses against pathogenic infections, allergic conditions, and malignancies and thus contain rich information about the immune status of the body. Rapid isolation of WBCs directly from whole blood is a prerequisite for any integrated immunoassay platform designed for examining WBC phenotypes and functions; however, such functionality is still challenging for blood-on-a-chip systems, as existing microfluidic cell sorting techniques are inadequate for efficiently processing unprocessed whole blood on chip with concurrent high throughput and cell purity. Herein we report a microfluidic chip for continuous-flow isolation and sorting of WBCs from whole blood with high throughput and separation efficiency. The microfluidic cell sorting chip leveraged the crossflow filtration scheme in conjunction with a surface-micromachined poly(dimethylsiloxane) (PDMS) microfiltration membrane (PMM) with high porosity. With a sample throughput of 1 mL h^{-1}, the microfluidic cell sorting chip could recover 27.4 ± 4.9% WBCs with a purity of 93.5 ± 0.5%. By virtue of its separation efficiency, ease of sample recovery, and high throughput enabled by its continuous-flow operation, the microfluidic cell sorting chip holds promise as an upstream component for blood sample preparation and analysis in integrated blood-on-a-chip systems.

Introduction

White blood cells (WBCs) in the blood and other body fluids contain rich information about the functionality of the human immune system and play a vital role in the diagnostics, prognostics, and treatments of diseases.[1] Recent progress in microfabrication and microfluidics has enabled minimization of traditional immunoassays involving WBCs with the aim of reducing sample consumption, shortening assay time, and minimizing human labor and intervention, while maintaining high sensitivity and multiplexing of traditional bulky assays.[2] However, while the emerging microfluidic technology has been successful in miniaturizing various types of immunoassays, most blood-on-a-chip systems require off-chip blood sample preparation, mainly due to a lack of on-chip capability for whole blood sample handling and preparation. Therefore, efficient and robust on-chip isolation of WBCs from unprocessed whole blood is critical and in an urgent need for highly integrated microfluidic immunoassay systems targeting and analyzing WBC functions and phenotypes.

Various attempts have been made to design microfluidic devices to separate WBCs from red blood cells (RBCs) in whole blood, based on their different physical, electrical, chemical, or functional properties.[3,4] However, very few techniques have been demonstrated successful in isolating WBCs efficiently from unprocessed whole blood,[5–12] owing to two major challenges associated with the high blood cell concentration and relatively low abundance of WBCs in blood. Specifically, WBCs are surrounded by abundant RBCs whose concentration is about 1000 times greater than that of WBCs. Consequently, microfluidic cell sorting devices must exhibit exceptionally high selectivity for WBCs over RBCs to ensure high WBC purity after sorting. Secondly, the blood cell concentration is extremely high (about 5×10^9 mL^{-1}), and blood cells fill up about half of the volume of blood (about 50% hematocrit). This high concentration of blood cells can easily cause clogging of microscale constrictions or filter structures designed for cell sorting in microfluidic devices, compromising their performance for on-chip applications involving whole blood samples.

---

[a] *Integrated Biosystems and Biomechanics Laboratory, University of Michigan, Ann Arbor, Michigan 48109, USA. E-mail: jpfu@umich.edu*
[b] *Department of Mechanical Engineering, University of Michigan, Ann Arbor, Michigan 48109, USA*
[c] *Department of Biomedical Engineering, University of Michigan, Ann Arbor, Michigan 48109, USA*

† Electronic supplementary information (ESI) available: See DOI: 10.1039/c4lc00350k

Size-based filtration methods using one-dimensional filters or two-dimensional membranes are among the most popular approaches for microfluidic cell sorting from whole blood.[3] Despite a variety of existing microfluidic filtration methods, none of the methods reported so far has been able to achieve high recovery rate, high purity, and high throughput simultaneously when processing whole blood samples. Wilding *et al.*, for example, used pillar- and weir-type microscale filters to trap WBCs while allowing RBCs to pass through.[10] Although the purity of isolated WBCs was high, the WBC recovery rate was <15%, and the device could only process 3.5 μL of whole blood due to clogging. Hosokawa *et al.* fabricated a microfiltration membrane made of electroformed nickel to isolate WBCs from blood specimens.[11] The device reported by Hosokawa *et al.* could recover >90% WBCs; however, only 1 μL of whole blood could be processed, again owing to membrane clogging. All of the aforementioned techniques were based on dead-end filtration; therefore, trapped WBCs were immobilized within microscale constrictions or filter structures, requiring an additional step to retrieve trapped WBCs for downstream analysis. To achieve continuous-flow isolation and sorting of WBCs from whole blood, VanDelinder *et al.* utilized the crossflow filtration principle for microfluidic cell sorting and successfully recovered 98% of WBCs with a purity of 70%.[12] The device reported by VanDelinder *et al.* was composed of a 25 μm-deep main channel and a series of 3 μm deep, 20 μm wide perfusion channels that were perpendicularly connected to the main channel. As the blood flew in the main channel, small RBCs were pushed to enter the perfusion channels by perfusion flow, with large WBCs contained and carried away in the main channel. However, the sample throughput of the device developed by VanDelinder *et al.* was still suboptimal (3.6 μL h^{-1}).

Over the last few years, there have been significant efforts in developing novel continuous-flow microfluidic blood cell sorting techniques to improve sample throughput for processing whole blood samples. The blood fractionation device based on deterministic hydrodynamics,[13] for example, could process whole blood at a throughput of 50 μL h^{-1}; however, the purity of isolated WBCs (<10%) was suboptimal for many important clinical applications. Another novel method termed affinity flow fractionation (AFF) utilized adhesion forces between target cells and cell adhesion molecules (CAMs) to separate neutrophils from whole blood.[14] While the AFF method could achieve a neutrophil purity of 92% after sorting, the improvement on sample throughput was still limited (~60 μL h^{-1}). Moreover, the AFF method depends on suitable CAMs that can allow transit interactions between target cells and the CAMs, which may limit its applications for other types of immune cells. The recently developed inertial microfluidics can operate at high flow rates and thus is a promising technique for high-throughput blood sample preparation.[15] Based on the concept of inertial microfluidics, a spiral inertial microfluidic cell sorter with a trapezoid cross-section was recently developed for isolation of immune cells from diluted whole blood.[16] The spiral inertial microfluidic cell sorter could process diluted blood of 0.5% hematocrit at an extremely high speed of 0.8 mL min^{-1}, equivalent to a throughput of ~600 μL h^{-1} for whole blood. The purity of the recovered WBCs after one-stage separation with the spiral inertial microfluidic cell sorter was moderate, but could improve to >90% utilizing two-stage separation with two spiral inertial microfluidic cell sorters operating sequentially.[16] Such two-stage separation, however, could limit the overall sample throughput and introduce design and operational complexities undesirable for integrated microfluidic blood analysis systems.

Herein we, for the first time, develop a microfluidic cell sorting chip that combines the advantages of the crossflow filtration scheme with a high porosity poly(dimethylsiloxane) (PDMS) microfiltration membrane (PMM). Wafer-scale fabrication of PMMs with large surface areas and high porosity has been recently demonstrated from our laboratory using a novel surface micromachining strategy.[17] Porosity of the PMM can be as high as 30%, with an effective surface area as large as 3 cm × 3 cm; both are favorable factors preventing clogging of the PMM when processing whole blood specimens. The surface-micromachined PMM is completely compatible with soft lithography techniques, which allow high flexibility in device design and ease of integration of the PMM with other PDMS-based microfluidic components. The crossflow filtration scheme contains a continuous tangential main flow to carry away WBCs and a crossflow that is perpendicular to the PMM to push undesired RBCs to pass across the PMM. The crossflow design further minimizes clogging and more importantly makes it possible for the continuous-flow operation of the microfluidic cell sorting chip.

The microfluidic cell sorting chip designed in this work leveraged the crossflow filtration scheme in conjunction with the PMM of high porosity to achieve continuous-flow sorting of WBCs from unprocessed whole blood. The microfluidic cell sorting chip achieved a sample throughput of 1 mL h^{-1} for processing undiluted whole blood specimens, the highest amongst current microfluidic blood cell sorting devices,[12–14,16] while preserving high recovery rate (27.4 ± 4.9%) and cell purity (93.5 ± 0.5%) for WBCs. This microfluidic cell sorting chip could be easily integrated with downstream custom designed microfluidic immunoassays to achieve highly integrated blood-on-a-chip analysis of the human immune status.

Methods and materials

Surface micromachining of PDMS microfiltration membrane (PMM)

The PDMS microfiltration membrane (PMM) was fabricated using a novel surface micromachining technique developed recently from our laboratory.[17] Briefly, silicon wafers were first silanized with (tridecafluoro-1,1,2,2,-tetrahydrooctyl)-1-trichlorosilane (United Chemical Technologies, Bristol, PA) for 1 h under a vacuum to facilitate subsequent release of patterned PMM layers. The PDMS precursor was prepared by thoroughly mixing the PDMS base and the curing agent (wt : wt = 1 : 10; Sylgard 184, Dow Corning, Midland, MI) before degassing in a vacuum desiccator for 30 min. The silicon wafers were then uniformly coated with 10 μm thick PDMS by spin coating the PDMS precursor at 500 rpm for 10 s and 7000 rpm for another 30 s. The silicon wafers were baked overnight at 60 °C for thermal curing of PDMS. The PDMS surface was activated by O_2 plasma (Harrick Plasma Cleaner, Harrick Plasma, Ithaca, NY) for 5–10 min right before the 10 μm thick AZ 9260 photoresist was spin coated at 500 rpm for 10 s followed by 2000 rpm for 30 s. The photoresist was baked at 80 °C for 10 min and gradually cooled down to room temperature (RT) for another 20 min. The photoresist was patterned by contact lithography, and the PMM was generated with reactive ion etching (RIE) (LAM 9400, Lam Research, Fremont, CA) using a SF_6 and O_2 gas mixture. Finally the photoresist was removed, and the PMM was baked overnight at 60 °C to allow the PDMS surface to recover to its original hydrophobic state.[18]

Design and fabrication of microfluidic cell sorting chip

Standard soft lithography was used to generate the top and bottom microfluidic channels for the microfluidic cell sorting chip.[19] Silicon molds were first fabricated using contact lithography and deep reactive ion etching (DRIE) (SPTS Pegasus, San Jose, CA) before silanized with (tridecafluoro-1,1,2,2,-tetrahydrooctyl)-1-trichlorosilane. The PDMS precursor (ratio of PDMS base to curing agent 1 : 10, wt : wt) was prepared and poured onto the silicon mold, followed by degassing in a vacuum desiccator for 30 min. The PDMS precursor was baked in a 60 °C oven overnight before peeling off the mold and cutting it into pieces. Holes for inlets and outlets were punched using a 1.2 mm diameter punch (Ted Pella, Redding, CA). PMM was then bonded with the top and bottom PDMS layers using plasma-assisted PDMS–PDMS bonding to form the completely sealed chip. Prior to separation assays, the microfluidic cell sorting chip was first flushed with 2% w/v Pluronic F-127 (Sigma-Aldrich, St. Louis, MO) for 1 h to render the PDMS channel non-adhesive. This treatment also helped prevent air bubbles forming within the chip.

In all chips tested in this work, the height of the top microfluidic channel was 100 μm, and the bottom microfluidic channel had a height of either 100 μm (version 1) or 200 μm (version 2). The top channel had a width of 500 μm, whereas the bottom channel had a width of 600 μm for alignment tolerance. The total channel length was 10 cm.

Numerical simulations

Finite element modeling was carried out using the commercial software COMSOL Multiphysics (COMSOL Inc., Burlington, MA). In our simulations, both the sample and sheath flows were considered as water with a density ρ of 1×10^3 kg m^{-3} and a dynamic viscosity μ of 1×10^{-3} Pa s.

To investigate the influence of misalignment between the sample and sheath inlets on flow pinching, we performed full-scale three-dimensional simulations using the convection and diffusion equations (Fig. 2A). Since neither the downstream microfluidic channel nor the PMM would affect the upstream flow field, we only calculated the flow field near the sample and sheath inlets to reduce computation load. Initial solute concentrations in the sample and sheath flows were set to be 1 and 0 mol m^{-3}, respectively. Diameters of the sample and sheath flow inlets were both 1.2 mm. The center-to-center distance between the two inlets and the distance from the sheath flow inlet center to the flow outlet were both 2 mm. The channel width and height were 500 μm and 100 μm, respectively. The sample and sheath flow rates ν_{sheath} and ν_{sample} were 2 mL h^{-1} and 4 mL h^{-1}, respectively. The position of the sample flow inlet was fixed in simulations, whereas the sheath flow inlet position was varied. The solute concentration profile at the outlet was analyzed.

A simplified two-dimensional model was used to simulate the flow field in the whole microfluidic cell sorting chip. The porous structure of the PMM was explicitly included in simulations, and the geometrical parameters used in the model had the exact values from the version 1 chip. The diameter and center-to-center distance of the holes in PMM was 4 μm and 12 μm, respectively. ν_{sample} in all cases was 2 mL h^{-1}, and ν_{sheath} was set to be 0 mL h^{-1} (no sheath flow), 2 mL h^{-1}, and 4 mL h^{-1}. The flow field throughout the whole chip was calculated first using the Navier–Stokes equations before a fixed amount of 3 μm particles was placed at the sample inlet for calculations of their trajectories using a particle tracing model. The particles were assumed to be sparse enough such that their presence had a negligible influence on the flow field. In the model, the particle motion was dominated by a drag force exerted by the fluid. The trajectories of the particles were calculated and thus the distribution of particles along the channel.

Cell culture and labeling

A human monocyte cell line from acute monocytic leukemia THP-1 (ATCC® TIB-202™) was used to mimic human WBCs. THP-1 cells were cultured following the manufacturer's instruction. Briefly, THP-1 cells were cultured in RPMI 1640 medium (Gibco, Grand Island, NY) supplemented with 10% v/v FBS (Gibco) and 0.05 mM 2-mercaptoethanol (Sigma-Aldrich). Cells were maintained in an incubator at 37 °C and 100% humidity. The culture medium was exchanged every 2–3 days, and the cells were passaged before reaching confluence. For visualization and cell counting, THP-1 cells were pre-stained with the CellTracker Green fluorescent dye (Molecular Probes, Grand Island, NY). CellTracker Green was directly added into the culture medium to a final concentration of 1 μM and incubated with cells at 37 °C for 10 min.

Cell viability was examined using Trypan Blue. Briefly, cell suspension was mixed with 0.4% Trypan Blue Stain (Gibco) at a ratio of 5 : 1. After 5 min of incubation at RT, cells were injected into a hemocytometer and observed under a phase contrast microscope (Carl Zeiss Microscopy GmbH, Jena, Germany). Cells that excluded the stain were classified as viable cells, whereas stained cells were identified as non-viable.

Separation of microbeads

Fluorescent polystyrene microbeads were purchased from Spherotech (Spherotech Inc., Lake Forest, IL). Two types of microbeads were used: one labeled with Nile red fluorophore and with a diameter of 3 μm and the other with light yellow fluorophore and a diameter of 11 μm. The sample flow contained the two types of microbeads both with a concentration of 1×10^6 mL^{-1} and was mixed thoroughly before being injected into the chip. Both sample and sheath flows (PBS buffer) were pushed into the chip at constant flow rates by using high-accuracy syringe pumps (KD Scientific, Holliston, MA). The chip was continuously monitored under a fluorescence microscope (Axio Observer, Carl Zeiss Microscopy GmbH). After both sample and sheath flows became stable, samples retrieved from the top and bottom outlets were collected using plastic vials for downstream analysis.

The recovery rate was defined as the ratio of the number of cells/beads retrieved from the top outlet to the number of cells/beads in the initial sample mixture

$$\text{Recovery rate} = n_{\text{out}}\, v_{\text{out}}/(n_{\text{in}}\, v_{\text{in}}) \qquad (1)$$

where n_{in} and n_{out} were the cell/particle concentration at the sample inlet and the top outlet, respectively, and v_{in} and v_{out} were the corresponding flow rates.

Separation of THP-1 cells spiked in blood samples containing only RBCs

WBC-depleted human blood, which contained only RBCs, was obtained from the University of Michigan Health System Blood Bank. To mimic whole blood, known quantities of fluorescence labeled THP-1 cells were spiked into WBC-depleted human blood, with the final concentrations of RBCs and WBCs at 5×10^9 mL^{-1} and 5×10^6 mL^{-1}, respectively, both comparable with their corresponding concentrations in whole blood.

The sample flow containing RBCs and spiked THP-1 cells and the sheath flow (PBS) were both pushed into the microfluidic cell sorting chip at constant flow rates. After both sample and sheath flows became stable, samples retrieved from the top and bottom outlets were collected using plastic vials for downstream analysis. Concentrations of THP-1 cells and RBCs recovered from the top outlet were quantified with a hemocytometer using both brightfield and fluorescence microscopes (Axio Observer, Carl Zeiss Microscopy GmbH). The purity of THP-1 cells was quantified as the percentage of cells retrieved from the top outlet that were THP-1 cells. The recovery rate of THP-1 cells was calculated using eqn (1).

Separation of WBCs from unprocessed whole blood

Porcine whole blood was obtained from the Department of Emergency Medicine at the University of Michigan Health System upon sacrificing pigs and was used the same day for separation assays, as prolonged blood storage could alter deformability of RBCs[20] and adversely affect separation results. To determine the WBC concentration in blood, the blood sample was lysed using 1× RBC lysis buffer (eBioscience, San Diego, CA) for 10 min. The remaining WBCs were counted using a hemocytometer under a brightfield microscope (Axio Observer, Carl Zeiss Microscopy GmbH). To determine the RBC number in blood, the blood sample was diluted by 1 : 1000, and the number of RBCs was counted by a hemocytometer using a brightfield microscope (Axio Observer, Carl Zeiss Microscopy GmbH).

The blood sample flow and the PBS sheath flow were pushed into the microfluidic cell sorting chip at constant flow rates. After both sample and sheath flows became stable, samples retrieved from the top and bottom outlets were collected using plastic vials for downstream analysis. To determine separation efficiency, the concentrations of WBCs and RBCs recovered from the top outlet were quantified using a hemocytometer *via* brightfield microscopy[7,8,12] (Axio Observer, Carl Zeiss Microscopy GmbH). The recovery rate of WBCs was calculated using eqn (1), and the purity of WBCs was defined as the percentage of cells recovered from the top outlet that were WBCs.

Results and discussion

Chip design

To achieve continuous-flow separation of WBCs from blood samples, a crossflow filtration design was adopted in the microfluidic cell sorting chip in conjunction with our recently developed high-porosity PDMS microfiltration membrane (PMM). The crossflow filtration design contained a continuous main flow that was tangential to PMM to carry away WBCs that were larger than the PMM pore size and a crossflow that was perpendicular to PMM to push undesired, smaller RBCs to pass across PMM to the bottom channel (Fig. 1A). Although crossflow filtration is less efficient in capturing large particles compared to dead-end filtration, it offers two distinct advantages: (1) in crossflow filtration the large particles are washed away by the tangential main flow, thus minimizing clogging of the filtration membrane, a major issue in any filtration-based separation; and (2) the tangential main flow that carries away the large particles can serve as the inflow for downstream sensing and analytical components, allowing a convenient continuous-flow operation on the same chip.

The microfluidic cell sorting chip was composed of three layers: a top channel, a bottom channel, and PMM sandwiched between the two channels (Fig. 1A–D). The top channel was designed to be slightly narrower than the bottom channel to allow for misalignment tolerance (Fig. 1E & F). The precise design and control of the PMM pore size was critical for enhancing the recovery rate and purity of WBCs. To determine the ideal cut-off pore size, the size distribution of WBCs and RBCs were first quantified

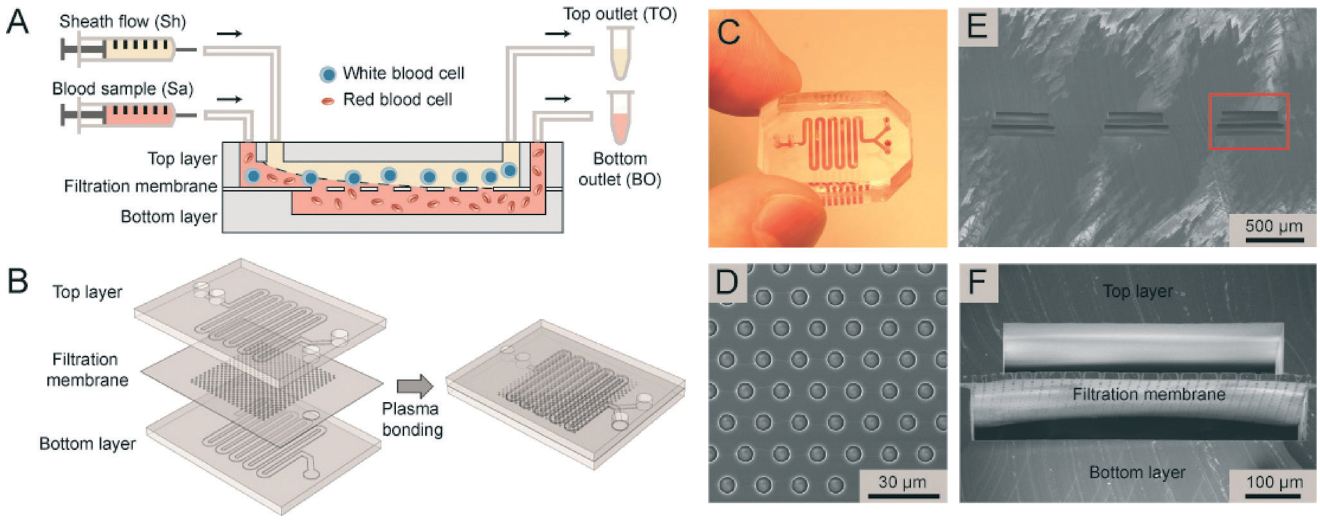

Fig. 1 Continuous-flow microfluidic cell sorting using crossflow filtration with PDMS microfiltration membranes (PMMs). (A) Schematic showing the PDMS microfluidic device structure and the principle of crossflow filtration. The device consisted of top and bottom microfluidic channels and PMM sandwiched in between. A sheath flow (Sh) injected downstream of the blood sample flow (Sa) pushed the sample flow downward into the bottom channel, so that cells smaller than the membrane pore size would pass across the PMM and exit through the bottom outlet (BO), whereas cells larger than the membrane pore would stay in the top channel and be carried away by the tangential flow to the top outlet (TO). (B) Schematic showing assembly of the three-layered PDMS device using plasma-assisted PDMS–PDMS bonding, with PMM sandwiched between the top and bottom PDMS layers. A serpentine channel design was used to increase the total channel length and thus cell sorting efficiency. (C) Photograph of the PDMS microfluidic device filled with a dye solution for visualization. (D) SEM image showing PMM containing a hexagonal array of holes with a pore diameter of 4 μm and a pore center-to-center distance of 12 μm. (E & F) Cross-sectional SEM images showing the PMM sandwiched between the top and bottom PDMS layers. The red rectangle in E highlights the area in which F was taken. The width of the top channel (500 μm) was slightly less than that of the bottom channel (600 μm), to compensate for alignment inaccuracy during bonding. In this device the heights of the top and bottom channels were both 100 μm, and the thickness of PMM was 10 μm.

(Fig. S1†). The pore size of PMM for isolating WBCs from blood samples was 4 μm (Fig. 1D), smaller than the typical diameter of WBCs (7–10 μm) as well as that of RBCs (5–7 μm), as normal RBCs can readily pass across 4 μm constrictions owing to a great degree of deformability of RBCs.[21] The pores on PMM were arranged as a hexagonal array with a pore center-to-center distance of 12 μm (Fig. 1D). Thus, the porosity of PMM used in this work for blood cell separation was about 10%. For comparison, the conventional track-etched polycarbonate filter has a reported porosity of less than 2%, while the other more recently developed parylene micropore membrane has a porosity of about 7%.[22–24] The surface area of PMM used in this work was 1 cm × 1 cm, enabling high-throughput separation of WBCs from blood specimens. To maximize the channel length, both the top and bottom channels had a serpentine shape such that the total channel length was 10 cm (Fig. 1B & C). The precisely controlled pore size and great porosity of PMM, the long separation channel, and the crossflow filtration scheme are all favorable factors contributing to high-throughput separation of WBCs from blood specimens with high recovery rate and purity.

The microfluidic cell sorting chip had two sequential inlets: the sample flow inlet was on the far left, and the sheath flow was injected from the second inlet from the left (the sheath flow inlet) to generate flow pinching and crossflow across PMM (Fig. 1A). The diameter of both the sample and sheath flow inlets was 1.2 mm, 2.8 times greater than the top channel width (500 μm), to ensure that the sample flow was always below the sheath flow when they encounter.[25] Thus, when the sample flow arrived at the sheath flow inlet, it was effectively pushed downward by the sheath flow to pass across PMM. While smaller cells or particles could pass across PMM without obstruction, cells or particles larger than the PMM pore would be confined in the top channel and carried away by the tangential main flow to the top outlet, thus achieving efficient continuous-flow separation.

Flow field simulations

To validate separation performance, we conducted finite element analysis to compute the flow field as well as particle trajectories inside the microfluidic cell sorting chip. In the first simulation, we only considered the sample and sheath flow inlets to verify the flow pinching effect due to sheath flow (Fig. 2A). The flow field was governed by the Navier–Stokes equations for incompressible fluid

$$\rho\left(\frac{\partial v}{\partial t}\right) + v\nabla v = -\nabla p + \mu\nabla^2 v \qquad (2)$$

$$\nabla \cdot v = 0 \qquad (3)$$

where v and p were denoted as fluid velocity and pressure, respectively. Mixing of the sample and sheath flows was

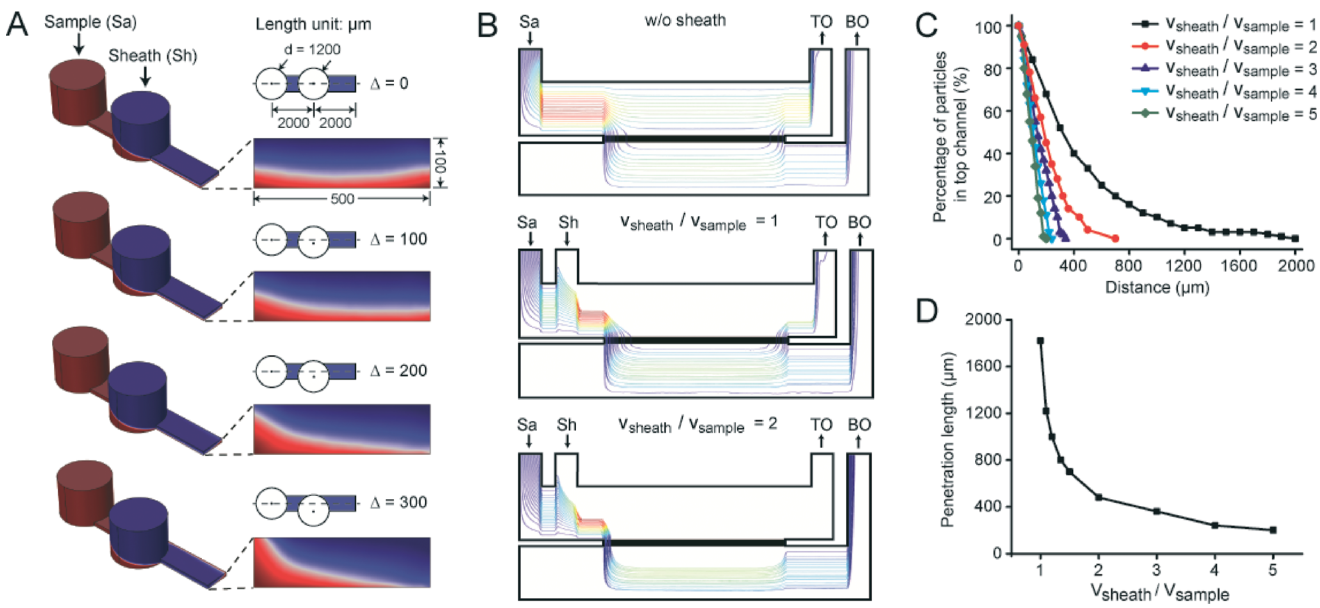

Fig. 2 Finite element analysis of microfluidic cell sorting. (A) Three-dimensional finite element simulations of the flow field at sample and sheath flow inlets. When the two inlets were in perfect alignment with the channel (Δ = 0 μm, where Δ is the side shift of the sheath inlet from the centerline of the channel), the sample flow (Sa; red) was uniformly pushed downward by the sheath flow (Sh; blue). As the misalignment between the two inlets increased (Δ = 100, 200, and 300 μm), the flow focusing effect caused by the sheath flow weakened. Dimensions of inlets and microfluidic channel were included in the figure. (B) Trajectories of particles in the microfluidic device simulated using a simplified two-dimensional model. Without sheath flow, particles smaller than the PMM pore size were evenly distributed in the top and bottom microfluidic channels and eluted through both the top and bottom outlets (top). With sheath flow, the majority of particles were forced to pass across PMM and elude from the bottom outlet (middle). When the ratio between the sheath and sample flow rates ($V_{\text{sheath}}/V_{\text{sample}}$) increased to 2, virtually all particles would exit *via* the bottom outlet (bottom). The porous structure of PMM was explicitly included in the simulations, and the geometrical parameters used in the model had the exact values from the version 1 chip. Dimensions are not to scale. (C) Percentage of particles in the top channel as a function of channel distance and $V_{\text{sheath}}/V_{\text{sample}}$. (D) Penetration length, defined as the channel distance at which all particles had passed across PMM, decreased as $V_{\text{sheath}}/V_{\text{sample}}$ increased.

governed by the convection diffusion equation

$$\frac{\partial c}{\partial t} = D\nabla^2 c - v\nabla c \qquad (4)$$

where D and c were the diffusion coefficient and solution concentration, respectively.

For simplicity, we treated both the sample and sheath flows as water and assigned them different solute concentrations. We also assumed that the downstream separation channels and PMM had no effect on the upstream flow field. When the two inlets and the channel had a perfect alignment (Δ = 0 μm), our simulation showed that the sample flow was uniformly pushed downward by the sheath flow, demonstrating effective flow pinching (Fig. 2A). Since the two inlets were manually generated using a hand-held puncher and the inlets might not be perfectly aligned with the center of the channel, we used numerical simulations to investigate the effect of inlet misalignment on flow pinching (Fig. 2A). As inlet misalignment increased and Δ = 100 μm, the flow pinching effect weakened, but the sample flow was still compressed downward to the lower part of the channel. If misalignment continued to increase (Δ = 200 or 300 μm), a portion of the sample flow would stay in the upper part of the channel, and flow pinching would fail. Based on the simulation results and the fact that manual alignment by hand during hole punching could achieve an accuracy of less than 100 μm, we conclude that the current chip design is capable of achieving effective flow pinching, critical for crossflow filtration with PMM.

In the second simulation, we investigated the effect of sheath flow on separation. Since PMM had high porosity, which could significantly increase computation load, we simulated the flow field and particle trajectories using a simplified two-dimensional model. In this model, major geometrical features of the microfluidic cell sorting chip were preserved, including heights of the top and bottom channels (100 μm), channel length (10 cm), PMM pore diameter (4 μm) and center-to-center distance (12 μm), and diameters of inlets and outlets (1.2 mm). The flow field was computed first using the Navier–Stokes equations before trajectories of 3 μm particles were extracted. The particles were evenly distributed in the top and bottom channels without any sheath flow (v_{sheath} = 0) (Fig. 2B, top). All particles were forced to pass across PMM to enter the bottom channel within the first 2 mm of the channel when $v_{\text{sheath}}/v_{\text{sample}}$ = 1 (Fig. 2B, center); however, some particles flowed back to the top channel before exiting the chip. When $v_{\text{sheath}}/v_{\text{sample}}$ = 2, all particles were pushed down to the bottom channel and exited *via* the bottom outlet (Fig. 2B, bottom).

To quantify separation efficiency, we recorded the number of particles remaining in the top channel at different distances from the beginning of the separation channel. An increasing proportion of particles passed across PMM as the distance increased, leading to a rapid decrease of the percentage of particles remaining in the top channel (Fig. 2C). In addition, the greater the sheath flow rate v_{sheath} as compared to the sample flow rate v_{sample}, the better the separation efficiency, as evidenced by the rapid decrease of the curves showing the percentage of particles remaining in the top channel (Fig. 2C) and the smaller penetration length, defined as the distance at which all particles passed across PMM to enter the bottom channel (Fig. 2D). Together, our simulations confirm that sheath flow would play a vital role in crossflow filtration and a relatively large sheath flow would enhance separation efficiency in the microfluidic cell sorting chip.

Separation of microbeads

To validate separation performance of the microfluidic cell sorting chip, we first used the chip to separate two different sized microbeads with diameters of 3 μm (yellow) and 11 μm (blue). The two types of microbeads were thoroughly mixed with an equal concentration of 1×10^6 mL^{-1} before injected into the chip at a constant flow rate. The microbeads were collected from the top and bottom outlets before examined and counted under a fluorescence microscope. The total sample volume processed in each experiment was 100 μL. Prior to collecting microbeads at the chip outlets, we waited for 5 min after the onset of each experiment to allow the flow to stabilize in the chip. For all assays performed, the microfluidic cell sorting chip could continuously operate for at least 30 min before initial clogging of PMM became observable under a brightfield microscope.

In Fig. 3A, fluorescence microscopic images illustrated the initial microbead mixture (left) and microbead solutions collected at the top (middle) and bottom (right) outlets when v_{sample} = 2 mL h^{-1} and v_{sheath} = 4 mL h^{-1}. Before separation, the microbead mixture contained an equal amount of 3 μm (yellow) and 11 μm (blue) beads. After separation, 97.3 ± 0.5% of 3 μm microbeads were removed from the solution collected at the top outlet, whereas 96.9 ± 0.4% of 11 μm microbeads remained. Consistently, the solution recovered from the bottom outlet contained only 3 μm microbeads without any 11 μm beads detectable under a fluorescence microscope (Fig. 3A).

We further examined the effect of v_{sample} and v_{sheath} on microbead separation. We gradually increased v_{sheath} from

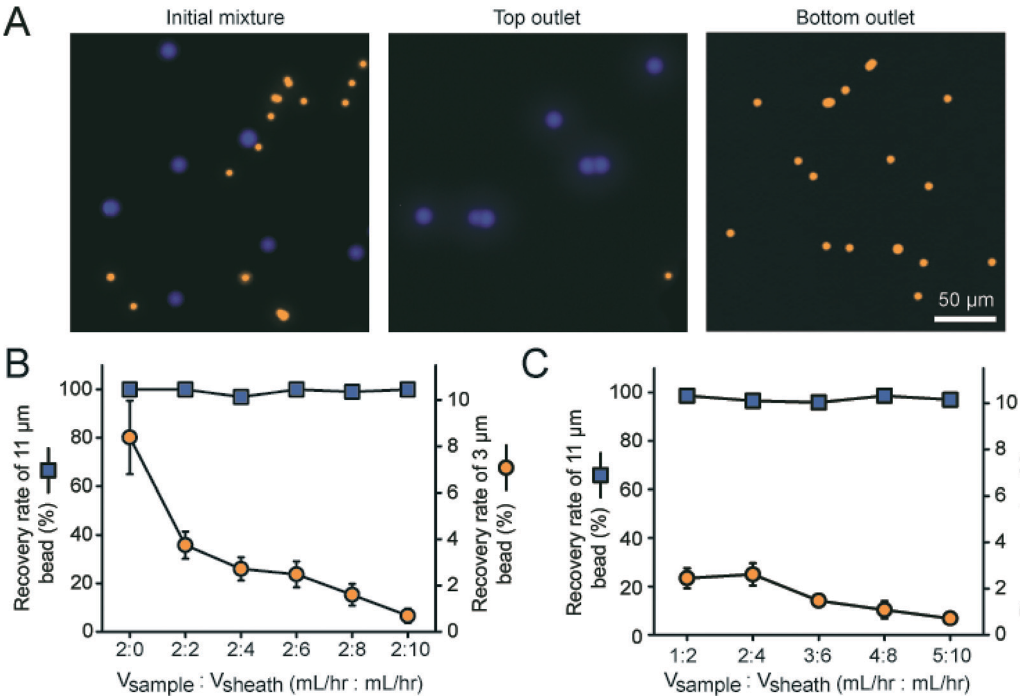

Fig. 3 Characterization of separation performance using different sized microbeads. (A) Representative fluorescence microscopic images showing the initial mixture of two different sized microbeads (11 μm *vs.* 3 μm) before separation (left) and the beads collected from the top (middle) and bottom (right) outlets after separation. The 11 μm microbeads are in blue, and the 3 μm ones are in yellow. Pores on PMM had a diameter of 4 μm and a center-to-center distance of 12 μm. (B) Recovery rates of microbeads at the top outlet, with V_{sample} = 2 mL h^{-1} and V_{sheath} from 0 to 10 mL h^{-1}. Under all conditions, >97% of 11 μm beads were retrieved from the top outlet. In contrast, the recovery rate of 3 μm beads decreased rapidly from 8.4 ± 1.6% to 0.7 ± 0.3% as V_{sheath} increased from 0 to 10 mL h^{-1}. (C) Recovery rates of microbeads at the top outlet, with the sample and sheath flow rates proportionally increasing from 1 mL h^{-1} : 2 mL h^{-1} to 5 mL h^{-1} : 10 mL h^{-1}. Under all conditions, the recovery rate of 11 μm microbeads was >97%, whereas the recovery percentage of 3 μm beads slightly decreased from 2.5 ± 0.5% to 0.7 ± 0.1% as the sample and sheath flow rates increased. The data in B & C represent the mean ± s.e.m with $n \geq 3$. Error bars for 11 μm microbeads were smaller than the symbol and thus were not plotted.

0 mL h^{-1} (no sheath flow) to 10 mL h^{-1}, while keeping v_{sample} constant at 2 mL h^{-1} (Fig. 3B). Under all conditions, >97% of 11 μm beads remained in the top channel and exited through the top outlet, whereas the number of 3 μm beads eluting from the top outlet decreased rapidly from 8.4 ± 1.6% to 0.7 ± 0.3% as v_{sheath} increased from 0 mL h^{-1} to 10 mL h^{-1}. We proportionally increased $v_{\text{sample}}/v_{\text{sheath}}$ from 1 : 2 to 5 : 10 (mL h^{-1} : mL h^{-1}) (Fig. 3C). Under all conditions, the recovery rate of 11 μm microbeads from the top outlet was >97%, whereas the recovery rate of 3 μm beads slightly decreased from 2.5 ± 0.5% to 0.7 ± 0.1% as $v_{\text{sample}}/v_{\text{sheath}}$ increased from 1 : 2 to 5 : 10 (mL h^{-1} : mL h^{-1}).

Separation of THP-1 cells spiked in blood mimicking samples

To further validate the microfluidic cell sorting chip, we prepared blood mimicking samples by spiking known quantities of human monocyte cells, THP-1 cells, into WBC-depleted human blood (Fig. 4A). Final concentrations of THP-1 cells and RBCs in the blood mimicking sample were 5 × 10^{6} mL^{-1} and 5 × 10^{9} mL^{-1}, respectively, comparable to their respective values in undiluted whole blood. For visualization and cell counting, THP-1 cells were pre-stained with CellTracker Green before spiked into WBC-depleted human blood. The total sample volume processed in each experiment was 100 μL.

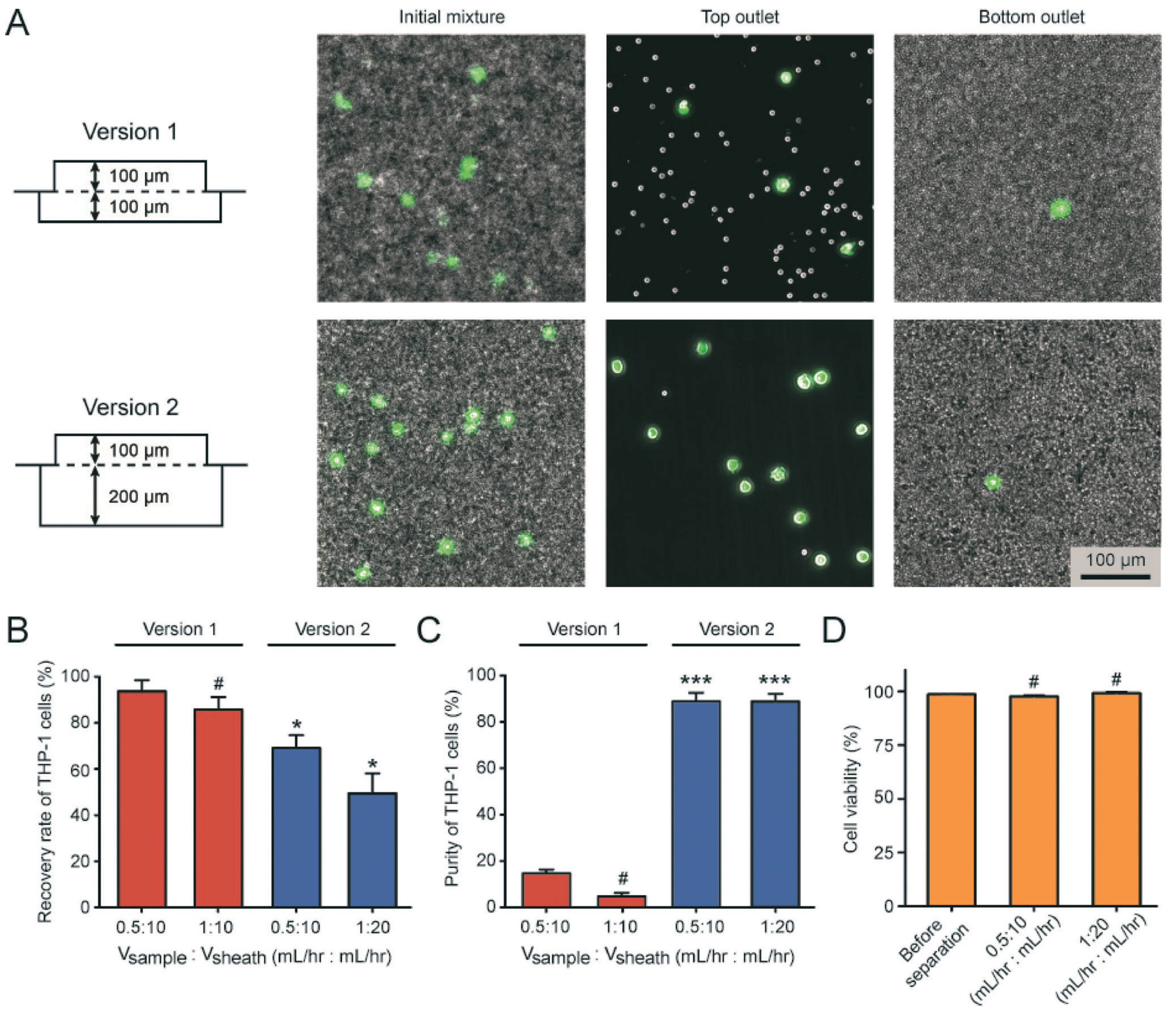

Fig. 4 Separation of white blood cells spiked in blood samples containing only red blood cells. (A) Representative fluorescence microscopic images showing the initial cell mixture before separation (left) and cells collected from the top (middle) and bottom (right) outlets after separation. THP-1 cells were pre-labeled with CellTracker Green before spiked into blood samples containing only RBCs. Images shown in the top and bottom rows were obtained from two versions of microfluidic devices that differed only in the bottom channel height (version 1: 100 μm; version 2: 200 μm). (B & C) Recovery rate and cell purity of THP-1 cells retrieved from the top outlet as a function of $V_{\text{sample}} : V_{\text{sheath}}$. (D) Viability of THP-1 cells before and after separation. The data in B–D represent the mean ± s.e.m with $n \geq 3$. P-values were calculated using two-side unpaired student t-tests. $^{\#}$, $P > 0.05$; *, $P < 0.05$; ***, $P < 0.001$.

Prior to collecting cells at the chip outlets, we waited for 5 min after the onset of each experiment to allow the flow to stabilize in the chip.

As expected, the initial blood mimicking sample contained extremely densely packed RBCs interspersed with spiked THP-1 cells (Fig. 4A). After separation using the microfluidic chip with the top and bottom channel heights of 100 μm and ν_{sample} = 0.5 mL h^{-1} and ν_{sheath} = 10 mL h^{-1}, the RBC concentration recovered from the top outlet was drastically reduced by 400 folds to 1.2×10^7 mL^{-1} (Fig. 4A). In contrast, the sample obtained from the bottom outlet contained mostly RBCs with very few THP-1 cells, suggesting that the sheath flow pushed only RBCs to pass across PMM, and all THP-1 cells were retained in the top channel (Fig. 4A). We varied ν_{sample} from 0.5 mL h^{-1} to 1 mL h^{-1} while keeping ν_{sheath} constant at 10 mL h^{-1}. The recovery rate of THP-1 cells decreased from 93.4 ± 4.6% to 86.2 ± 6.2% as ν_{sample} increased from 0.5 mL h^{-1} to 1 mL h^{-1} (Fig. 4B). The purity of THP-1 cells was 14.8 ± 3.9% and 4.8 ± 1.5% for ν_{sample} = 0.5 mL h^{-1} and ν_{sample} = 1 mL h^{-1}, respectively (Fig. 4C).

It is noteworthy that THP-1 cells were observed to pass across PMM within the first 2 cm along the separation channel, much longer than predicted in simulations for microbeads. This discrepancy is mainly due to the simplicity of the one-dimensional model used for simulations of microbead trajectories in the microfluidic cell sorting chip. Another contributing factor is that in the simulations the microbeads are assumed to be perfectly circular and rigid, and their effect on the flow field is negligible. For assays using blood cells, the shape of blood cells could change, especially when passing across PMM, and the cell–cell and cell–flow interactions could also be important in dictating cell transport during the crossflow filtration process.

To improve cell purity, we increased the bottom channel height of the microfluidic cell sorting chip to 200 μm while keeping all other geometrical factors unchanged (version 2; Fig. 4A). Increased bottom channel height significantly enhanced the purity of THP-1 cells after separation, owing to smaller flow resistance of the bottom channel and thus an enhanced crossflow and an increased likelihood for each blood cell in the top channel to be filtered by PMM. Accordingly, the fraction of total flow ($\nu_{\text{sample}} + \nu_{\text{sheath}}$) in the top channel decreased from 13.9% (version 1) to 8.2% (version 2) (data not shown). Indeed, for the version 2 chip, the purity of THP-1 cells was improved to 88.9 ± 3.6% with ν_{sample} = 0.5 mL h^{-1} and ν_{sheath} = 10 mL h^{-1} and 88.7 ± 3.4% with ν_{sample} = 1 mL h^{-1} and ν_{sheath} = 20 mL h^{-1}(Fig. 4C), which was 5 times greater compared to the chip with a bottom channel height of 100 μm. Improvements of THP-1 cell purity was accompanied with a slight decrease of THP-1 cell recovery rate (69.1 ± 5.5% with ν_{sample} = 0.5 mL h^{-1} and ν_{sheath} = 10 mL h^{-1}; 49.3 ± 8.8% with ν_{sample} = 1 mL h^{-1} and ν_{sheath} = 20 mL h^{-1}) (Fig. 4B), which could be attributed to an enhanced crossflow forcing more THP-1 cells to pass across PMM.

We further compared viability of THP-1 cells before and after separation using the microfluidic cell sorting chip with a bottom channel height of 200 μm. Under all flow conditions, the viability of THP-1 cells recovered from separation was constantly as high as 98%, comparable to the cells before separation (Fig. 4D), suggesting the negligible adverse effect of microfluidic cell sorting on cell viability.

Separation of WBCs from unprocessed whole blood

Blood mimicking samples using THP-1 cells spiked in WBC-depleted human blood allowed characterization of separation performance of the microfluidic cell sorting chip for blood specimens. However, on average the diameter of THP-1 cells was significantly greater than that of WBCs (Fig. S1†). We therefore sought to further apply the version 2 of the microfluidic cell sorting chip for separation of WBCs from unprocessed porcine whole blood. Blood sorting was performed with ν_{sample} = 0.5 mL h^{-1} and ν_{sample} = 10 mL h^{-1} or ν_{sample} = 1 mL h^{-1} and ν_{sample} = 20 mL h^{-1}. Further increasing the sample and sheath flow rates might lead to device leakage. Blood cells (including both WBCs and RBCs) collected from the top outlet were examined and counted under a phase contrast microscope. WBCs were identified by their relatively larger size compared to RBCs (Fig. 5A). Concentrations of WBCs and RBCs retrieved from the top outlet were compared with their initial values in unprocessed porcine blood, in order to calculate cell recovery rate and purity. The recovery rate of WBCs was 46.4 ± 1.8% when ν_{sample} = 0.5 mL h^{-1} and ν_{sheath} = 10 mL h^{-1} and decreased to 27 ± 4.9% when ν_{sample} = 1 mL h^{-1} and ν_{sheath} = 20 mL h^{-1} (Fig. 5B). Both values were lower than recovery rates achieved for THP-1 cells spiked in blood mimicking samples under the same flow conditions, which could be attributed to the smaller size of porcine WBCs as compared to THP-1 cells (Fig. S1†). Excitingly, the purity of WBCs collected from the top outlet was 65.2 ± 5.1% when ν_{sample} = 0.5 mL h^{-1} and ν_{sample} = 10 mL h^{-1} and further increased to 93.5 ± 0.5% when ν_{sample} = 1 mL h^{-1} and ν_{sample} = 20 mL h^{-1} (Fig. 5C). We postulate that a greater flow rate makes it easier for both RBCs and WBCs to pass across PMM; but such an effect might be stronger for the smaller and more deformable RBCs, leading to heightened purity of WBCs after separation. We repeated cell viability assays for WBCs before and after separation, with data showing that microfluidic cell sorting had no significant effect on WBC viability (Fig. 5D).

Conclusion

In this paper we demonstrated a microfluidic cell sorting chip that could achieve continuous-flow separation of WBCs from unprocessed whole blood with high throughput and cell purity. The microfluidic cell sorting chip functions based on the crossflow filtration principle in conjunction with flow pinching and PMM with high porosity. We utilized numerical simulations to verify the working principle and optimize the operational conditions of the microfluidic cell sorting chip. We carefully validated separation performance of the chip under different flow conditions and using different samples,

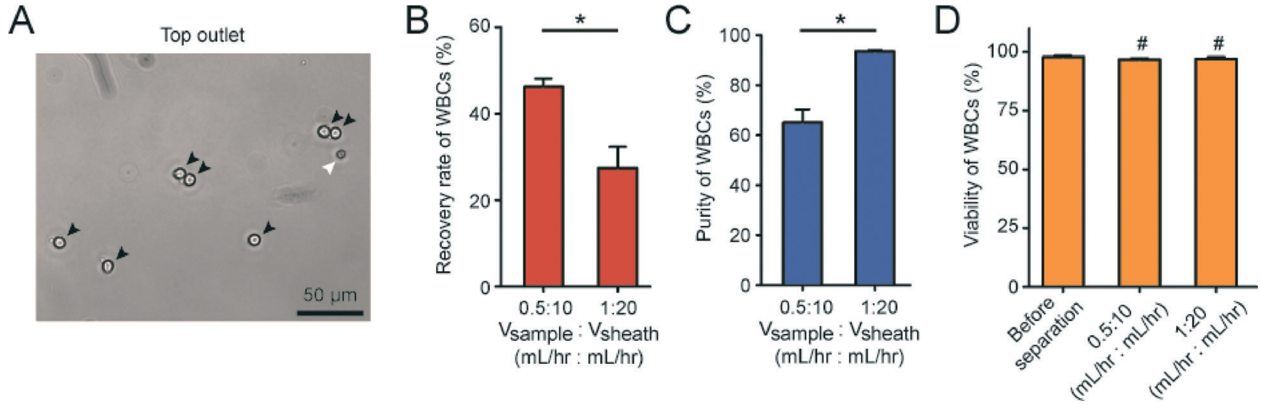

Fig. 5 Separation of WBCs from unprocessed whole blood. (A) Representative bright-field image showing blood cells collected from the top outlet after separation of unprocessed whole blood samples using the version 2 microfluidic device. WBCs (black arrow head) were identified by their relatively larger size compared to RBCs (white arrow head). (B & C) Recovery rate and purity of WBCs collected at the top outlet as a function of V_{sample} and V_{sheath}. (D) Viability of WBCs before and after separation. The data in B–D represent the mean ± s.e.m with $n \geq 3$. P-values were calculated using two-side unpaired student t-tests. $^{\#}$, $P > 0.05$; *, $P < 0.05$.

including microbead mixtures, THP-1 cells spiked in blood mimicking samples, and unprocessed whole blood. When processing unprocessed whole blood, the microfluidic cell sorting chip recovered 27.4 ± 4.9% WBCs with a purity as high as 93.5 ± 0.5% at a sample throughput of 1 mL h^{-1}, the highest value amongst currently reported microfluidic blood fractionation systems.[12–14,16]

The unique design of the microfluidic cell sorting chip enables four important features highly desirable for blood-on-a-chip analysis. Firstly, the microfluidic cell sorting chip demonstrated its capability for continuous-flow sorting of WBCs from unprocessed whole blood with high throughput and purity, both critical for downstream on-chip phenotypic and functional analysis of WBCs. The high purity of isolated WBCs minimizes the influence of contaminating cells and enhances the reliability and the signal-to-noise ratio of downstream on-chip immunoassays involving WBCs. Secondly, the microfluidic cell sorting chip could directly handle unprocessed whole blood at a sample throughput as high as 1 mL h^{-1}. Such a heightened throughput is important for rapid and efficient blood-on-a-chip analysis for clinical applications, where it is common to collect several milliliters of blood from patients. Thirdly, by virtue of its separation efficiency, ease of sample recovery and high throughput enabled by its continuous-flow operation, the microfluidic blood sorting chip holds great promise as an upstream component for blood sample preparation and analysis in integrated blood-on-a-chip systems. The continuous-flow operation makes it convenient to integrate the cell sorting chip with downstream microfluidic immunoassay platforms, thereby enabling a highly integrated and automated blood-on-a-chip system. Finally, the crossflow filtration principle in conjunction with high-porosity PMM could be adapted for separation of other blood components useful for blood-based clinical analysis and diagnosis, such as platelets and blood plasma, by varying the pore size of PMM. It is also possible for the microfluidic cell sorting chip to isolate different subtypes of immune cells (such as CD4+ or CD8+ T-cells), by using microbeads coated with antibodies to recognize and capture target cells expressing specific antibodies from blood specimens, before injecting the blood sample into the microfluidic cell sorting chip.[26] With all of these highly desirable features, we envision that the microfluidic cell sorting chip demonstrated in this work can serve as a standard cell sorting component for upstream sample preparation in future highly integrated blood-on-a-chip systems.

Acknowledgements

We acknowledge financial support for this work from the National Science Foundation (ECCS 1231826 and CBET 1263889), the National Institutes of Health (1R01HL119542), and the Department of Mechanical Engineering at the University of Michigan, Ann Arbor. We thank Theresa Downs from the Department of Pathology at the University of Michigan for providing blood samples. The Lurie Nanofabrication Facility at the University of Michigan, a member of the National Nanotechnology Infrastructure Network (NNIN) funded by the National Science Foundation, is acknowledged for support in microfabrication.

References

1 P. J. Delves and I. M. Roitt, *N. Engl. J. Med.*, 2000, **343**, 37–49.
2 W. Chen, N.-T. Huang, X. Li, Z. T. F. Yu, K. Kurabayashi and J. Fu, *Front. Oncol.*, 2013, 3, 98.
3 Z. T. F. Yu, K. M. Aw Yong and J. Fu, *Small*, 2014, **10**, 1687–1703.
4 H. W. Hou, A. A. S. Bhagat, W. C. Lee, S. Huang, J. Han and C. T. Lim, *Micromachines*, 2011, **2**, 319–343.
5 J. A. Davis, D. W. Inglis, K. J. Morton, D. A. Lawrence, L. R. Huang, S. Y. Chou, J. C. Sturm and R. H. Austin, *Proc. Natl. Acad. Sci. U. S. A.*, 2006, **103**, 14779–14784.

6 M. Yamada, M. Nakashima and M. Seki, *Anal. Chem.*, 2004, **76**, 5465–5471.

7 S. S. Shevkoplyas, T. Yoshida, L. L. Munn and M. W. Bitensky, *Anal. Chem.*, 2005, 77, 933–937.

8 M. Tsukamoto, S. Taira, S. Yamamura, Y. Morita, N. Nagatani, Y. Takamura and E. Tamiya, *Analyst*, 2009, **134**, 1994–1998.

9 P. Sethu, M. Anahtar, L. L. Moldawer, R. G. Tompkins and M. Toner, *Anal. Chem.*, 2004, **76**, 6247–6253.

10 P. Wilding, L. J. Kricka, J. Cheng, G. Hvichia, M. A. Shoffner and P. Fortina, *Anal. Biochem.*, 1998, **257**, 95–100.

11 M. Hosokawa, M. Asami, S. Nakamura, T. Yoshino, N. Tsujimura, M. Takahashi, S. Nakasono, T. Tanaka and T. Matsunaga, *Biotechnol. Bioeng.*, 2012, **109**, 2017–2024.

12 V. VanDelinder and A. Groisman, *Anal. Chem.*, 2007, **79**, 2023–2030.

13 J. A. Davis, D. W. Inglis, K. J. Morton, D. A. Lawrence, L. R. Huang, S. Y. Chou, J. C. Sturm and R. H. Austin, *Proc. Natl. Acad. Sci. U. S. A.*, 2006, **103**, 14779–14784.

14 S. Bose, R. Singh, M. Hanewich-Hollatz, C. Shen, C.-H. Lee, D. M. Dorfman, J. M. Karp and R. Karnik, *Sci. Rep.*, 2013, **3**, 2329.

15 D. Di Carlo, *Lab Chip*, 2009, **9**, 3038–3046.

16 L. Wu, G. Guan, H. W. Hou, A. A. S. Bhagat and J. Han, *Anal. Chem.*, 2012, **84**, 9324–9331.

17 W. Chen, R. H. Lam and J. Fu, *Lab Chip*, 2012, **12**, 391–395.

18 D. Bodas and C. Khan-Malek, *Sens. Actuators, B*, 2007, **123**, 368–373.

19 J. R. Anderson, D. T. Chiu, H. Wu, O. J. Schueller and G. M. Whitesides, *Electrophoresis*, 2000, **21**, 27–40.

20 T. L. Berezina, S. B. Zaets, C. Morgan, C. R. Spillert, M. Kamiyama, Z. Spolarics, E. A. Deitch and G. W. Machiedo, *J. Surg. Res.*, 2002, **102**, 6–12.

21 J. P. Shelby, J. White, K. Ganesan, P. K. Rathod and D. T. Chiu, *Proc. Natl. Acad. Sci. U. S. A.*, 2003, **100**, 14618–14622.

22 G. Vona, A. Sabile, M. Louha, V. Sitruk, S. Romana, K. Schutze, F. Capron, D. Franco, M. Pazzagli, M. Vekemans, B. Lacour, C. Brechot and P. Paterlini-Brechot, *Am. J. Pathol.*, 2000, **156**, 57–63.

23 H. K. Lin, S. Zheng, A. J. Williams, M. Balic, S. Groshen, H. I. Scher, M. Fleisher, W. Stadler, R. H. Datar, Y. C. Tai and R. J. Cote, *Clin. Cancer Res.*, 2010, **16**, 5011–5018.

24 S. Zheng, H. K. Lin, B. Lu, A. Williams, R. Datar, R. J. Cote and Y. C. Tai, *Biomed. Microdevices*, 2011, **13**, 203–213.

25 M. Rhee, P. M. Valencia, M. I. Rodriguez, R. Langer, O. C. Farokhzad and R. Karnik, *Adv. Mater.*, 2011, **23**, H79–H83.

26 W. Chen, N. T. Huang, B. Oh, R. H. Lam, R. Fan, T. T. Cornell, T. P. Shanley, K. Kurabayashi and J. Fu, *Adv. Healthcare Mater.*, 2013, **2**, 965–975.